

Revealing the High Energy Emission from the Obscured Seyfert Galaxy MCG -5-23-16 with *Suzaku*

James N. REEVES^{1,2} Hisamitsu AWAKI³ Gulab C. DEWANGAN⁴ Andy C. FABIAN⁵ Yasushi FUKAZAWA⁶
Luigi GALLO^{7,8} Richard GRIFFITHS⁴ Hajime INOUE⁸ Hideyo KUNIEDA^{8,9} Alex MARKOWITZ¹
Giovanni MINIUTTI⁵ Tsunefumi MIZUNO⁶ Richard MUSHOTZKY¹ Takashi OKAJIMA^{1,2} Andy PTAK^{1,2}
Tadayuki TAKAHASHI⁸ Yuichi TERASHIMA^{3,8} Masayoshi USHIO⁸ Shin WATANABE⁸ Tomonori YAMASAKI⁶
Makoto YAMAUCHI¹⁰ and Tahir YAQOOB^{1,2}

¹*Exploration of the Universe Division, Code 662, NASA Goddard Space Flight Center, Greenbelt Road,
Greenbelt, MD 20771, USA
jnr@milkyway.gsfc.nasa.gov*

²*Department of Physics and Astronomy, Johns Hopkins University, 3400 N Charles Street,
Baltimore, MD 21218, USA*

³*Department of Physics, Ehime University, Matsuyama 790-8577, Japan*

⁴*Department of Physics, Carnegie Mellon University, 5000 Forbes Avenue, Pittsburgh,
PA 15213, USA*

⁵*Institute of Astronomy, University of Cambridge, Madingley Road, Cambridge,
CB3 0HA, UK*

⁶*Department of Physics, Hiroshima University, 1-3-1 Kagamiyama, Higashi-Hiroshima,
Hiroshima 739-8526, Japan*

⁷*Max-Planck-Institut für extraterrestrische Physik, Postfach 1312, Garching, Germany*

⁸*Institute of Space and Astronautical Science, Japan Aerospace Exploration Agency, Yoshinodai 3-1-1,
Sagamihara, Kanagawa 229-8510, Japan*

⁹*Department of Physics, Nagoya University, Furo-cho, Chikusa, Nagoya 464-8602, Japan*

¹⁰*Department of Applied Physics, University of Miyazaki, 1-1, Gakuen-Kibanadai-Nishi,
Miyazaki 889-2192, Japan*

(Received 2006 July 27; accepted 2006 September 18)

Abstract

We report on a 100 ks *Suzaku* observation of the bright, nearby ($z = 0.008486$) Seyfert 1.9 galaxy MCG -5-23-16. The broad-band (0.4–100 keV) X-ray spectrum allows us to determine the nature of the high energy emission with little ambiguity. The X-ray continuum consists of a cutoff power-law of photon index $\Gamma = 1.9$, absorbed through Compton-thin matter of column density $N_{\text{H}} = 1.6 \times 10^{22} \text{ cm}^{-2}$. A soft excess is observed below 1 keV and is likely a combination of emission from scattered continuum photons and distant photoionized gas. The iron K line profile is complex, showing narrow neutral iron $K\alpha$ and $K\beta$ emission, as well as a broad line which can be modeled by a moderately inclined accretion disk. The line profile shows either the disk is truncated at a few tens of gravitational radii, or the disk emissivity profile is relatively flat. A strong Compton reflection component is detected above 10 keV, which is best modeled by a combination of reflection off distant matter and the accretion disk. The reflection component does not appear to vary. The overall picture is that this Seyfert 1.9 galaxy is viewed at moderate ($\sim 50^\circ$) inclination through Compton-thin matter at the edge of a Compton-thick torus covering $\sim 2\pi$ steradians, consistent with unified models.

Key words: galaxies: individual (MCG -5-23-16); galaxies: active; galaxies: Seyfert; X-rays: galaxies

1. Introduction

Determining the origin of the iron K emission line is one of the fundamental issues in high energy research on Active Galactic Nuclei, as it is regarded as the most direct probe available of the inner accretion disk and black hole. Indeed the iron line diagnostic in AGN first became important during the Ginga era, showing that the 6.4 keV iron $K\alpha$ emission line was common amongst Seyfert galaxies (Pounds et al. 1990). The associated reflection hump above 10 keV, produced by Compton down-scattering of

higher energy photons, showed the iron line emission arises from Compton-thick material, possibly the accretion disk (Lightman & White 1988; George & Fabian 1991). The higher (CCD) resolution spectra available with ASCA appeared to indicate that the iron line profiles were broad and asymmetrically skewed (to lower energies), which was interpreted as evidence that the majority of the line emission originated from the inner accretion disk around the massive black hole (Tanaka et al. 1995; Nandra et al. 1997; Reynolds 1997).

The picture emerging from the study of the iron K line

with XMM-Newton and Chandra is much more complex. The presence of a narrower 6.4 keV iron emission component, from more distant matter (e.g. the outer disk, BLR or the molecular torus) is commonplace in many type I AGN (Yaqoob & Padmanabhan 2004; Page et al. 2004). In contrast the broad, relativistic component of the iron line profile appears to be weaker than anticipated and in some cases may be absent altogether, e.g. NGC 5548 (Pounds et al. 2003a); NGC 4151 (Schurch et al. 2003).

Furthermore, it is possible that complex absorption in some objects may also effect the modeling of the iron K-line and reduce its strength; e.g. in NGC 3783 (Reeves et al. 2003) and NGC 3516 (Turner et al. 2005). The possible presence of the reflection component hardening the spectrum towards higher energies (George & Fabian 1991) can also complicate fitting the broad iron K line, if bandpass above 10 keV is not available. This is where new observations with Suzaku can provide an important breakthrough, by determining the underlying AGN continuum emission over a wide bandpass (e.g. from 0.3 keV to > 100 keV), thereby resolving the ambiguities present in fitting the iron K-shell band.

MCG-5-23-16 is an X-ray bright, nearby ($z = 0.008486$ or 36 Mpc, Wegner et al. 2003) AGN that is classed optically as a Seyfert 1.9 galaxy (Veron et al. 1980) and is known to possess moderate absorption in the soft X-ray band (Mushotzky 1982). It is one of the brightest Seyfert galaxies in the 2-10 keV band, with a historically typical flux of $7 - 10 \times 10^{-11} \text{ erg cm}^{-2} \text{ s}^{-1}$ (Mattson & Weaver 2004), which makes it an ideal object to study in the iron K band and at high energies to measure any Compton reflection component. Indeed of the objects that now show evidence for a broad redshifted iron K line, MCG-5-23-16 appears to be one of the more robust examples from XMM-Newton data (Dewangan et al. 2003; Balestra et al. 2004) or with ASCA (Weaver et al. 1997).

Here we report on a 100 ks observation of MCG-5-23-16, performed in December 2005 with Suzaku (Mitsuda et al. 2006). In Section 2, the Suzaku observations of MCG-5-23-16 are outlined, whilst in Section 3 the detailed modeling of the time-averaged spectrum is performed. In Section 4 the variability of the iron line and reflection component are compared while in Section 5, modeling of the reflection component is discussed.

2. The Suzaku Observation of MCG-5-23-16

MCG-5-23-16 was observed by Suzaku between 7-10 December 2001 with a total duration of 220 ks (see Table 1 for a summary of observations). Events files from version 0.7 of the Suzaku pipeline processing were used. ¹

¹ Version 0 processing is a simplified processing applied to the Suzaku data obtained during the SWG phase, for the purpose of establishing the detector calibration as quick as possible. Some processes that are not critical for most of the initial scientific studies, e.g., aspect correction, fine tuning of the event time tagging of the XIS data, are skipped in version 0 processing, and hence, the quality of the products is limited in these directions,

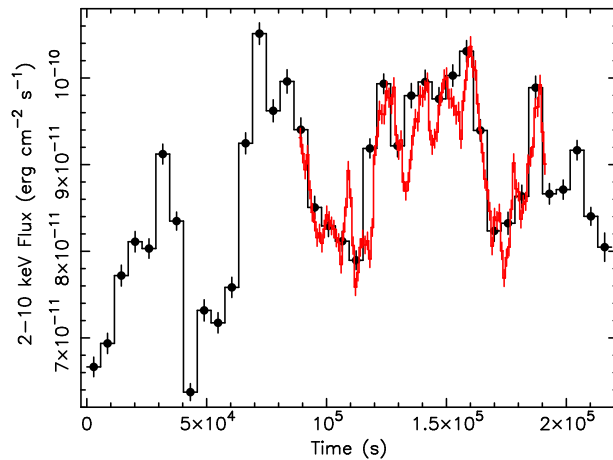


Fig. 1. The 2-10 keV XIS3 lightcurve of MCG-5-23-16, shown as black circles. The observation started on 7 December 2005, with a total exposure time (after screening) of ~ 100 ks. The Suzaku lightcurve has been binned into orbital length bins of 5760s. Overlaid in red is the XMM-Newton EPIC-pn lightcurve, which is simultaneous for part of the observation.

All events files were further screened within XSELECT to exclude data within the SAA (South Atlantic Anomaly) as well as excluding data with an Earth elevation angle (ELV) < 5 degrees. Data with Earth day-time elevation angles (DYE-ELV) less than 20 degrees were also excluded. Furthermore data within 256s of the SAA were excluded from the XIS and within 500s of the SAA for the HXD (using the T_SAA_HXD parameter within the house-keeping files). Cut-off rigidity (COR) criteria of > 8 GeV/c for the HXD data and > 6 GeV/c for the XIS were used.

2.1. XIS Data Analysis

For the XIS, only good events with grades 0,2,3,4 and 6 were used, while hot and flickering pixels were removed from the XIS images using the CLEAN SIS script. Time intervals effected by telemetry saturation were also removed. The XIS was set to normal clocking mode and the data format was either in the 3×3 or 5×5 edit modes (corresponding to 9 and 25 pixel pulse height arrays respectively that are telemetered to the ground). The XIS pulse height data for each X-ray event were converted to PI (Pulse Invariant) channels using the XISPI software version 2005/12/26 and CTI parameters were used from 2006/05/22.

The 4 XIS source spectra (see Koyama et al. (2006) for details of the XIS) were extracted from circular source regions of $4.34'$ (6mm) radius centered on the source, which was observed off-axis in the HXD nominal pointing position. Background spectra were extracted from three $2.5'$ circles offset from the source region. The source and background extraction regions were also chosen to avoid the calibration sources on the corners of the CCD chips. XIS

compared with the official data supplied to the guest observers. As of 2006 July, version 0.7 is the latest, where the absolute energy scale of ~ 5 eV is achieved for the XIS data.

Table 1. Summary of Observations

Instrument	TSTART (UT)	TSTOP (UT)	Exposure (ks)
Suzaku/XIS	2005/12/07 22:59:49	2005/12/10 11:48:54	98.1
Suzaku/PIN	2005/12/07 22:40:00	2005/12/10 11:50:50	71.4
Suzaku/GSO	2005/12/07 22:40:00	2005/12/10 11:50:50	18.3
XMM-Newton/PN	2005/12/08 21:11:33	2005/12/10 06:57:51	96.2
Chandra/HETG	2005/12/08 17:41:30	2005/12/09 02:33:59	
Chandra/HETG	2005/12/09 20:52:11	2005/12/10 03:00:10	49.5
RXTE/PCA	2005/12/09 13:16:00	2005/12/09 20:30:00	12.8
Swift/XRT	2005/12/09 00:03:00	2005/12/09 09:54:57	10.1

response files (rmfs) provided by the instrument teams were used (dated 2006/02/13), while ancillary response files (arfs) appropriate for the HXD nominal pointing were chosen dated as of 2006/04/15, matching the size (6mm) of the source extraction regions used. For the front illuminated XIS chips (XIS 0,2,3) data over the energy range 0.6–10 keV were used, while for the softer back-illuminated XIS 1 chip data from 0.4–8 keV were used. Data around the CCD Si K edge from 1.7–1.95 keV were ignored in all 4 XIS chips, due to uncertain calibration at this energy at the time of writing. A total source exposure (after screening) of 98.1 ks was obtained for the 4 XIS chips. The 2–10 keV source lightcurve for the XIS 3 is shown in Figure 1.

The XIS spectra were corrected for the hydrocarbon ($C_{24}H_{38}O_4$) contamination on the optical blocking filter, by including an extra absorption column due to Carbon and Oxygen in all the spectral fits. The column densities for each detector were calculated based on the date of the observation and the off-axis position of the source. The Carbon column densities (N_C) used were 1.64×10^{18} , 2.18×10^{18} , 2.82×10^{18} and 4.40×10^{18} atoms cm^{-2} for XIS 0,1,2,3 respectively, with the ratio of C/O column densities set to 6. The additional soft X-ray absorption due to the hydrocarbon contamination was included as a fixed spectral component using the VARABS absorption model in all the spectral fits.

The net source count rates obtained for the 4 XIS detectors are 2.843 ± 0.006 counts s^{-1} , 3.081 ± 0.006 counts s^{-1} , 3.403 ± 0.007 counts s^{-1} and 3.316 ± 0.007 counts s^{-1} for XIS 0–3 respectively, with background typically 1% of the source rate. Given the large number of source counts available in the observation, the XIS source spectra were binned to a minimum of 200 counts per bin to enable the use of the χ^2 minimization technique.

2.2. HXD Data Analysis

2.2.1. HXD/PIN

The source spectrum was extracted from the cleaned HXD/PIN events files, processed with the screening criteria described above. The HXD/PIN instrumental background spectrum was generated from a time dependent model provided by the HXD instrument team. The model utilized the count rate of upper discriminators as the measure of cosmic-ray flux that passes through the silicon PIN diode and provide background spectra based upon

a database of non-X-ray background observations made by the PIN diode to date (Kokubun et al. 2006). Both the source and background spectra were made with identical GTIs (good time intervals) and the source exposure was corrected for detector deadtime (which is $< 5\%$). A detailed description of the PIN detector deadtime is given in Kokubun et al. (2006). The net exposure time of the PIN source spectrum was 71.4 ks after deadtime correction. Note that the background spectral model was generated with $10\times$ the actual background count rate in order to minimize the photon noise on the background; this has been accounted for by increasing the effective exposure time of the background spectra by a factor of $\times 10$. The HXD/PIN response file dated 2006/08/14 for the HXD nominal position was used for these spectral fits. Instrumental and performance details of the HXD are discussed in Takahashi et al. (2006) and Kokubun et al. (2006).

In addition a spectrum of the cosmic X-ray background (CXB) (Boltdt 1987; Gruber et al. 1999) was also simulated with the HXD/PIN. The form of the CXB was taken as $9.0 \times 10^{-9} \times (E/3 \text{ keV})^{-0.29} \times e^{(-E/40 \text{ keV})}$ erg $cm^{-2} s^{-1} sr^{-1} keV^{-1}$. When normalized to the field of view of the HXD/PIN instrument the effective flux of the CXB component is 9.0×10^{-12} erg $cm^{-2} s^{-1}$ in the 12–50 keV band. Note the flux of MCG -5-23-16 measured by the HXD over the same band is 1.6×10^{-10} erg $cm^{-2} s^{-1}$, i.e. the CXB component represents only 6% of the net source flux measured by the HXD/PIN. Note that there is some uncertainty in the absolute flux level of the CXB component measured between missions, for instance Churazov et al. (2006) find the CXB normalization from *Integral* to be about 10% higher than measured by Gruber et al. (1999) from the HEAO-1 data. However this level of uncertainty is much smaller than the net source flux of MCG -5-23-16, at the level of $< 1\%$. Furthermore the spatial fluctuation of the CXB also has a negligible effect ($< 1\%$ of the net source flux), for instance Kushino et al. (2002) measure a $6.5 \pm 0.6\%$ fluctuation based on the 2–10 keV ASCA GIS data, which has a total field of view similar to Suzaku HXD/PIN.

The HXD/PIN spectrum is shown in Figure 2, plotted from 12–50 keV. At present we exclude the HXD/PIN data above 50 keV, as a detailed study of the background systematics for HXD/PIN is on-going above this energy. Figure 2 shows the total (source + observed background)

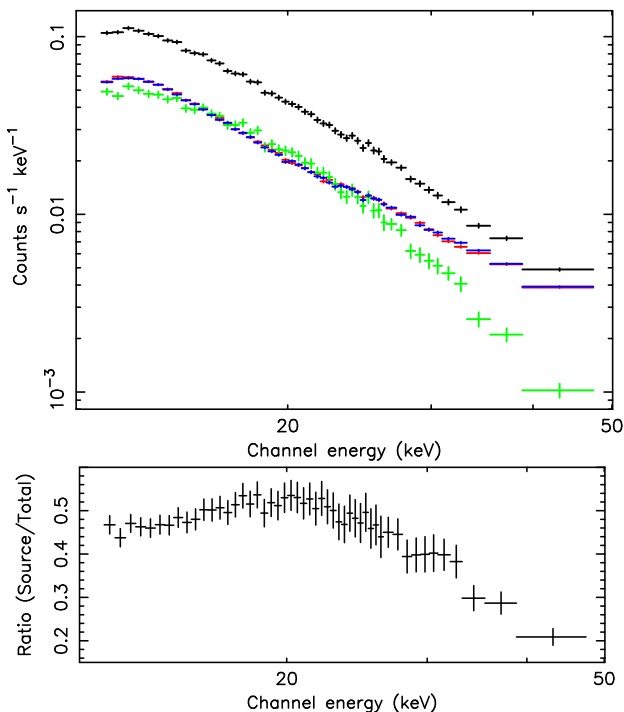


Fig. 2. HXD/PIN spectra for the Suzaku observation of MCG-5-23-16. The upper panel shows the total spectrum (source plus background, black). The points in red and blue show two independent background models for HXD/PIN, the red points are the ones adopted in the paper. The two backgrounds show very good agreement. The net source counts (i.e. total minus model background) are shown in green. Note the source is detected in each data bin at a minimum of 10σ above the background. The lower panel shows the ratio of net source spectrum to the total spectrum, which is $> 20\%$ over the 12–50 keV range.

spectrum and two independent background model spectra provided by the HXD instrument team (the red and blue points), both of which include the instrumental (non X-ray) background and the contribution from the CXB. The net source spectrum is plotted (green points), which shows the total spectrum minus the background model spectrum (the red points are the background model adopted in this paper). The agreement between the two independent background models is excellent, the spectral fits derived for MCG-5-23-16 produces consistent results (within the statistical errors quoted in the paper) for each background model. The lower panel of Figure 2 shows the ratio of net source counts to the total observed PIN counts. Thus the net source counts are $> 20\%$ of the total counts for each bin from 12–50 keV, while the source is detected at $> 10\sigma$ above the background in each bin in the spectrum. The resulting net PIN source count rate from 12–50 keV was $0.454 \pm 0.003 \text{ counts s}^{-1}$, compared to the PIN background rate of $0.494 \pm 0.001 \text{ counts s}^{-1}$.

2.2.2. HXD/GSO

For the HXD/GSO, background spectra were extracted from a Suzaku observation of the cluster Abell 1795 which occurred from December 10–13, 2005, just after the MCG-

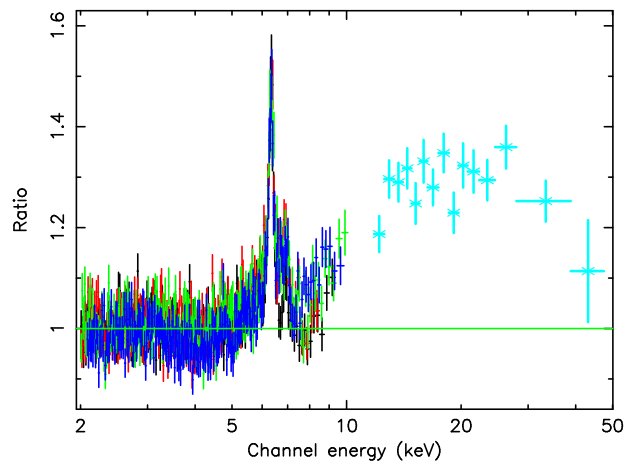


Fig. 3. The four Suzaku XIS spectra (XIS 0, black; XIS 1, red; XIS 2; green; XIS 3; blue) and HXD/PIN (light blue stars) over the 2–50 keV range plotted as a ratio to an absorbed power-law of photon index $\Gamma = 1.8$. A 15% cross-normalization factor has been accounted for between HXD/PIN and the XIS (the HXD/PIN is thought to be 13–15% higher with the current calibration). The cross-normalization between the 4 XIS detectors above 2 keV agrees within 5% and the photon index is consistent within $\Gamma = \pm 0.05$ for the 4 XIS spectra. There is an excess of counts above 12 keV in the HXD/PIN compared to the XIS, most likely due to a Compton reflection hump.

5-23-16 observation. Abell 1795 was not detected in the HXD/GSO and is therefore suitable for use as a background template given the close proximity in time of the two observations. Both the GSO background from Abell 1795 and the MCG-5-23-16 source spectra were extracted from orbits that contained no SAA passage, which have the most reliable (and least variable) GSO background. Matching orbits (i.e. at the same time of day) were also chosen between the MCG-5-23-16 and Abell 1795 observations. After applying this additional screening, the net exposure times for the GSO source and background spectra were then 18.3 ks and 28.6 ks respectively. The source was detected at the 15σ statistical level over the GSO background in the 50–100 keV band and at a level of 5.5% over the detector background. As a study of the background systematics of the GSO is still on-going, unless otherwise stated we do not include the GSO data in the subsequent spectral fits. Nonetheless a plot of the GSO detection between 50–100 keV and of the HXD/PIN and XIS spectra is shown in Figure 4, compared to an absorbed power-law spectrum (see description later). Above 100 keV the GSO background systematics are more uncertain and subject to further study, so a reliable detection of this source above this energy cannot be made at the present time.

2.3. Simultaneous Observations With Other Observatories

Simultaneous observations were also conducted with XMM-Newton, Chandra (HETG), RXTE and Swift covering part of the Suzaku observation. The details of the observations are shown in Table 1. Figure 1 shows the

lightcurve from Suzaku XIS3 compared to the XMM-Newton EPIC-pn observation, with the 100ks XMM-Newton observation overlapping with part of the Suzaku observation. The PATTERN=0 data only were used for the EPIC-pn. A more detailed description of the analysis of the simultaneous observations will appear in a subsequent paper (Braitto et al. 2006, in preparation); the purpose of this paper is to describe the Suzaku observation especially the properties of the iron K line and the hard X-ray emission and reflection component above 10 keV. Nonetheless we refer below to the Chandra HETG data for the measurement of the width of the iron $K\alpha$ line core, to XMM-Newton to check the consistency of the iron K line profile with Suzaku and to RXTE as an independent check of the reflection component.

3. Broad-Band X-ray Spectral Analysis

3.1. Initial Spectral Fitting

We first concentrate our analysis on the time-averaged MCG -5-23-16 spectrum, from the whole Suzaku observation. The XIS and HXD/PIN background subtracted spectra were fitted using XSPEC v11.3, including data over the energy range 0.4–50 keV. A Galactic absorption column of $N_H = 8.0 \times 10^{20} \text{ cm}^{-2}$ (Dickey & Lockman 1990) was included in all the fits and spectral parameters are quoted in the rest-frame of MCG -5-23-16 at $z = 0.008486$. All errors are quoted at 90% confidence for one interesting parameter (corresponding to $\Delta\chi^2 = 2.7$) unless otherwise stated. A cosmology of $H_0 = 70 \text{ km s}^{-1} \text{ Mpc}^{-1}$ and $\Lambda_0 = 0.73$ is assumed throughout.

Initially we fitted the 4 XIS spectra and HXD data using a simple absorbed power-law model in the 2–5 keV band in order for the continuum parameters not to be affected by the iron $K\alpha$ line at 6.4 keV, the reflection component at high energies, as well as any soft X-ray spectral complexity below 1 keV. The continuum was fitted with a photon index $\Gamma \sim 1.8$ and an absorption column of $1.6 \times 10^{22} \text{ cm}^{-2}$. The relative normalization of the HXD/PIN was initially fixed at 15% above that of the XIS, as has been found to date from calibration observations of the Crab (Kokubun et al. 2006). Figure 3 shows the spectrum and data/model ratio of the 4 XIS spectra as well as the HXD/PIN data between 2–50 keV against the absorbed power-law continuum. The photon indices of the 4 XIS spectra are all in good agreement to within ± 0.05 of each other; these are $\Gamma = 1.84 \pm 0.03$ (for XIS 0), $\Gamma = 1.79 \pm 0.04$ (XIS 1), $\Gamma = 1.82 \pm 0.03$ (XIS 2) and $\Gamma = 1.82 \pm 0.03$ (XIS 3). The cross normalization between all 4 XIS detectors is also in good agreement to $\pm 5\%$. An excess of flux in the HXD/PIN compared to the XIS spectra is clearly apparent.

Due to the good agreement between the XIS spectra, data from the three front illuminated XIS 0, XIS 2 and XIS 3 chips were co-added (hereafter referred to as XIS FI) in order to maximize signal to noise. We do not combine the XIS 1 which is a back illuminated chip and its response is better suited to the soft X-ray spectrum, with lower effective area at high energies. Figure 4 shows the

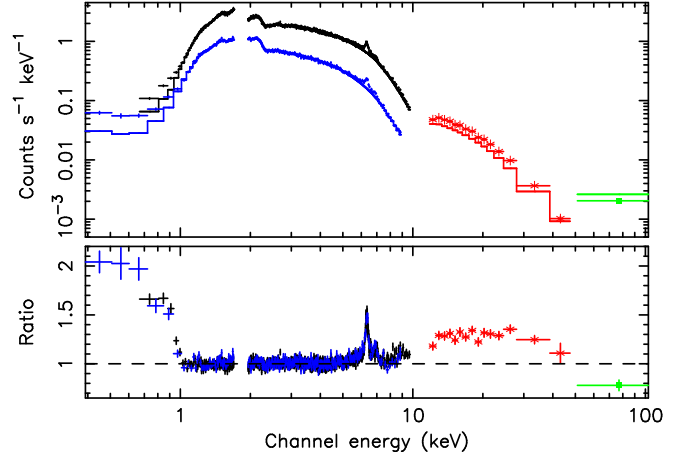


Fig. 4. The broad-band (0.4–100 keV) Suzaku spectrum of MCG -5-23-16. The upper panel shows the data, plotted against an absorbed power-law model of photon index $\Gamma = 1.8$ (solid line) and column density $1.6 \times 10^{22} \text{ cm}^{-2}$, fitted over the 2–5 keV band. The lower panel shows the data/model ratio residuals to this power-law fit. The data from XIS FI chips are shown in black, the XIS 1 in blue, the HXD/PIN as red stars and the HXD/GSO as green squares. Clear deviations in the iron K-shell band are apparent between 6–7 keV, while an excess of counts (due to a soft excess) is present below 1 keV. A hard excess is seen in the HXD spectrum above 10 keV, due to the presence of a reflection component in this object.

spectrum and data/model residuals to the entire Suzaku spectrum from XIS FI, XIS 1, HXD/PIN and HXD/GSO over the 0.4–100 keV range against the simple absorbed power-law model. Note we include the GSO datapoint here for comparison, but it is not used in the spectral fitting. An excess of counts above the power-law continuum is seen above 10 keV likely due to Compton reflection in the X-ray spectrum, while the spectrum appears to turn over at the very highest energies, perhaps due to a high energy exponential cut-off. At lower energies a soft excess is seen below 1 keV (especially in the softer XIS 1 instrument), which may be due to an unabsorbed component in scattered emission associated with this Seyfert 1.9 galaxy.

3.2. The Baseline Continuum Model

We then constructed a baseline model which can fit the spectrum of MCG -5-23-16. Initially we concentrated on the joint fit between XIS FI and HXD/PIN from 0.4–50 keV. For the continuum, we modeled the spectrum with an absorbed power-law component including an exponential cut-off at high energies of the form, $N_{\text{PL}} E^{-\Gamma} \times e^{-E/E_{\text{cut}}}$; where N_{PL} is the normalization of the power-law (in photons $\text{cm}^{-2} \text{ s}^{-1} \text{ keV}^{-1}$ at 1 keV), E is the energy (in keV), Γ is the photon index and E_{cut} is the e-folding cut-off energy (in keV).

This primary power-law continuum is absorbed by two layers of neutral gas; an absorbing layer at the redshift of MCG -5-23-16 and the Galactic absorption column of $8 \times 10^{20} \text{ cm}^{-2}$ (Dickey & Lockman 1990). A second soft X-ray power-law component was included, ab-

sorbed by only the Galactic column, in order to model the soft excess. Abundances were set those of Wilms et al. (2000) using the cross-sections of Balucinska-Church & McCammon (1992). Furthermore a reflection component produced by Compton down-scattering of X-rays off neutral material was included, using the PEXRAV model within XSPEC (Magdziarz & Zdziarski 1995). The reflection component is absorbed by the Galactic column only. The continuum parameters (Γ , N_{PL} and E_{cut}) were tied to those of the incident cut-off power-law. The inclination (θ) of the reflector was set to 45° , while the Fe abundance (A_{Fe}) was allowed to vary. The solid angle (Ω) subtended by the Compton reflector was determined by the parameter $R = \Omega/2\pi$. The best-fit parameters are shown in Table 2. The primary power-law has a photon index of $\Gamma = 1.95 \pm 0.03$ after the inclusion of the reflection component, with a high energy cut-off of $E_{\text{cut}} > 170$ keV, absorbed by a neutral column density of $N_{\text{H}} = 1.65 \pm 0.03 \times 10^{22} \text{ cm}^{-2}$. The soft, unabsorbed power-law required to fit the soft excess has a steeper photon index of $\Gamma = 3.1 \pm 0.3$. The properties of the iron K line and the reflection component are described below.

3.3. The Iron K Line Profile

The data/model residuals of the XISFI spectrum in the iron K band to this continuum model are shown in Figure 5 (without the inclusion of the reflection component). For comparison, the XMM-Newton EPIC-pn data are also plotted, which shows that the iron K line profiles obtained by XMM-Newton and Suzaku are in excellent agreement. The data from both missions show a strong iron $K\alpha$ core at 6.4 keV, an excess of counts both redwards and bluewards of 6.4 keV, a weak peak at 7 keV due to the iron $K\beta$ line and a drop at 7.1 keV, likely due to the neutral Fe K edge associated with the Compton reflector.

The iron K line profile was then fitted in several steps. Firstly Compton reflection was included, as described above. The resultant line profile to the Suzaku data can be seen in Figure 6, panel (a). Then the narrow core to the $K\alpha$ line was added to the model, while a narrow $K\beta$ line was also included, the line energy of the $K\beta$ line was fixed at 7.056 keV, with the line flux set equal to 12% of the $K\alpha$ as expected for neutral iron. For completeness, we also add a small Compton shoulder to the iron $K\alpha$ line, represented by a narrow Gaussian centered at 6.3 keV, with normalization fixed to 20% of the $K\alpha$ flux, expected if the emission originates from Compton-thick material (Matt 2002). After the inclusion of the narrow lines, a clear excess of counts in the Suzaku data can be seen around 6.4 keV (Figure 6, panel b). This excess can be modeled by either a broad Gaussian line or a diskline profile from an accretion disk (Fabian et al. 1989). Figure 6(c) shows the residuals in the iron K band after fitting the iron K line with the narrow $K\alpha$ and $K\beta$ lines, as well as a broad iron line component. The fit statistic obtained is good considering the high statistical quality of the data ($\chi^2/\text{dof} = 1983/1879$ for the disk-line model, where dof is the number of degrees of freedom).

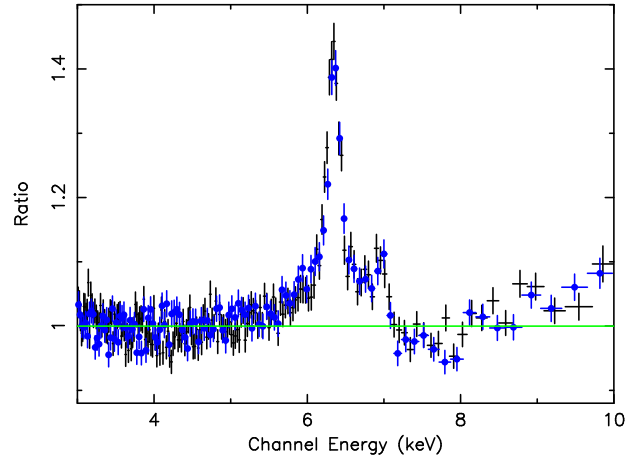


Fig. 5. The iron line profile of MCG -5-23-16, plotted as a ratio against a power-law of photon index $\Gamma = 1.8$. The data from Suzaku XIS FI is shown in black and for comparison the blue circles show the data from the XMM-Newton EPIC-pn observation. Both observations show a narrow iron $K\alpha$ core at 6.4 keV, a red-wing below 6.4 keV, a peak at 7.05 keV due to Fe $K\beta$. The edge at 7.1 keV is due to the reflection component.

3.3.1. The Narrow $K\alpha$ Line

The narrow $K\alpha$ core has an equivalent width of 70 ± 6 eV, centered at 6.391 ± 0.007 keV, with a measured width of $\sigma = 51 \pm 12$ eV. The ^{55}Fe calibration source located on the corners of the XIS chips can be used as an accurate calibrator of the energy and intrinsic width of the iron line. The ^{55}Fe source produces lines from Mn $K\alpha$ ($K\alpha_1$ & $K\alpha_2$ at 5.899 keV and 5.888 keV respectively with a branching ratio of 2:1). From measuring the lines in the calibration source, we find that the line energy is shifted redwards by 9 ± 2 eV, while there is some residual width (after the instrumental response function has been accounted for) in the calibration lines of $\sigma = 41 \pm 2$ eV. Therefore the intrinsic width (σ_{int}) of the iron $K\alpha$ line is simply $\sigma_{\text{int}}^2 = \sigma_{\text{meas}}^2 - \sigma_{\text{cal}}^2$ (where σ_{meas} is the measured width and σ_{cal} is the residual width of the calibration lines).

The intrinsic width is thus formally consistent with being unresolved, while a statistical upper limit can be placed on the width of $\sigma_{\text{int}} < 48$ eV, corresponding to a velocity width of $\sigma_v < 2200 \text{ km s}^{-1}$. The corrected energy of the narrow iron line is then 6.400 ± 0.007 keV, consistent with a superposition of the neutral $K\alpha_1$ and $K\alpha_2$ iron lines at 6.404 keV and 6.391 keV respectively. In comparison, the line width and energy obtained from the simultaneous Chandra/HETG observation are $\sigma < 43$ eV ($\sigma_v < 2000 \text{ km s}^{-1}$) and 6.405 ± 0.015 keV (Braitto et al. 2006) which is in excellent agreement. Note that the residual broadening in the XIS response function has a negligible effect on the broad line parameters determined below.

3.3.2. The Broad Iron Line

When modeled by a Gaussian, the broad component of the line is also centered near 6.4 keV ($E = 6.43 \pm 0.10$ keV), with an equivalent width of 62 ± 17 eV and an intrinsic

Table 2. Spectral Fit Parameters. Note ^a normalization of power-law in units 10^{-2} photons $\text{cm}^{-2} \text{s}^{-1} \text{keV}^{-1}$ at 1 keV; ^b X-ray flux in units of $10^{-11} \text{erg cm}^{-2} \text{s}^{-1}$; ^c column density in units of 10^{22}cm^{-2} ; ^d normalization (flux) of iron line in units 10^{-5} photons $\text{cm}^{-2} \text{s}^{-1}$; ^e inner disk radius in gravitational radii. ^f donates parameter is fixed in fit.

	Parameter	Mean	High	Low
Continuum	Γ	1.95 ± 0.03	1.92 ± 0.03	1.93 ± 0.03
	N_{PL}^a	3.2 ± 0.1	3.5 ± 0.1	2.6 ± 0.1
	E_{cut} (keV)	> 170	200^f	200^f
	Flux_{2-10}^b	8.76	9.91	7.12
	Flux_{15-100}^b	19.0	20.0	14.1
	N_{H}^c	1.65 ± 0.03		
Scattered	Γ	3.1 ± 0.3		
	N_{PL}^a	$1.5 \pm 0.2 \times 10^{-2}$		
Reflection	R	1.1 ± 0.2	1.2 ± 0.2	1.3 ± 0.2
	Abund (Fe)	0.40 ± 0.13	0.5^f	0.5^f
Narrow	E (keV)	6.400 ± 0.007	6.40 ± 0.01	6.40 ± 0.01
Gaussian	σ (eV)	< 48	10^f	10^f
	N_{line}^d	6.5 ± 0.5	6.5 ± 2.0	$5.4_{-2.6}^{+1.7}$
	EW (eV)	70 ± 6	65 ± 19	91_{-44}^{+28}
	E (keV)	6.39 ± 0.10	6.4 ± 0.1	6.4 ± 0.1
Broad	σ (keV)	0.44 ± 0.12	0.4^f	0.4^f
	N_{line}^d	6.1 ± 1.6	$5.6_{-3.6}^{+3.1}$	$6.8_{-2.9}^{+3.4}$
	EW (eV)	62 ± 17	53	92
	E (keV)	6.40^f		
or Diskline (XMM+Suzaku)	R_{in}^e	37_{-10}^{+25}		
	θ	53_{-9}^{+7}		
	N_{line}^d	5.1 ± 0.9		
	EW (eV)	60 ± 11		

width of $\sigma = 440 \pm 120 \text{eV}$ or $\sigma_v \sim 20000 \text{km s}^{-1}$. This large velocity indicates that the broad line must originate from close to the black hole in MCG -5-23-16. Therefore the broad iron line was modeled with an emission profile from an accretion disk around a Schwarzschild black hole (DISKLINE, Fabian et al. (1989)). The outer radius of the diskline was fixed to $400R_g$ (where $R_g = GM/c^2$), while it was assumed that the iron K emission originates from neutral matter at 6.4 keV. The disk emissivity is parameterized in the form r^{-q} , where q is the emissivity index and r is the disk radius. Initially the emissivity was fixed at $q = 3$. The disk inclination angle is then constrained to be $50_{-10}^{+32^\circ}$, the inner radius of the disk is $26_{-8}^{+35}R_g$, while the line EW is $63 \pm 16 \text{eV}$. If the constraint on the disk emissivity is relaxed, then a disk inner radius of $6R_g$ is allowed, with a flatter emissivity of $q = 2.0_{-0.7}^{+0.4}$. Overall the fit statistic is good, with $\chi^2/\text{dof} = 1983/1879$ (Table 3, model 1); if the broad line is not included and the data are refitted then the fit is considerably worse ($\chi^2/\text{dof} = 2027/1882$, Table 3, model 2). Thus the broad line is required in the data at $> 99.99\%$ confidence. We also note that a simple broad Gaussian profile produces a very slightly worse fit than a diskline profile ($\chi^2/\text{dof} = 1987/1879$). In order to obtain tighter constraints on the diskline, a combined fit was then performed with the Suzaku and XMM-Newton EPIC-pn data. For this fit the inner radius of the disk is $37_{-10}^{+25}R_g$ (for a fixed emissivity of $q = 3$), the inclination angle is $53_{-9}^{+7^\circ}$, while the line EW is $60 \pm 11 \text{eV}$. A

summary of the line parameters is shown in Table 2.

Finally it has been previously suggested from XMM-Newton studies of the iron line profile in AGN that complex absorption (either ionized or partially covering the X-ray source) could provide an alternative explanation for the relativistic iron line (Reeves et al. 2004; Pounds et al. 2004; Turner et al. 2005). In order to test this hypothesis we fitted an iron K-shell bound-free absorption edge constrained between 7.1–9.3 keV (the known energy range from FeI up to FeXXVI), in order to mimic the additional opacity of an ionized absorber in the iron K bandpass. While it was possible to fit a weak iron K-shell edge to the Suzaku data (at $7.2 \pm 0.1 \text{keV}$ with an optical depth of $\tau < 0.05$), the fit was considerably worse than for a diskline ($\chi^2/\text{dof} = 2020/1880$ with an edge vs. $\chi^2/\text{dof} = 1983/1879$ with a disk-line). Similarly we also attempted to fit the spectrum with a neutral partial covering absorber (the PCFABS model in XSPEC), which also resulted in a worse fit ($\chi^2/\text{dof} = 2020/1880$) with an absorption column of $\sim 5 \times 10^{22} \text{cm}^{-2}$ and a covering fraction of $\sim 10\%$. Note that there is no evidence for ionized absorption lines and/or edges from lighter elements below the iron K band, either from the Suzaku XIS spectrum, or from the XMM-Newton EPIC-pm and Chandra/HETG spectra (Braitto et al. 2006). Thus other than the neutral line of sight column density towards MCG -5-23-16 (of $1.6 \times 10^{22} \text{cm}^{-2}$) which has been included in the spectral model, there is no evidence of complex absorption

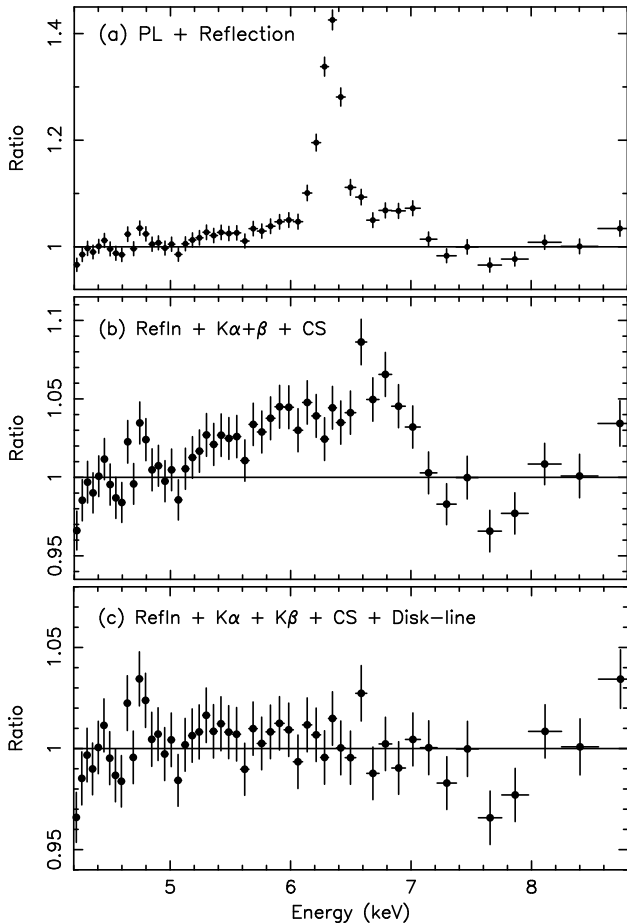


Fig. 6. Data/model ratio residuals of the spectrum of MCG-5-23-16, in the iron K-shell band. Panel (a) shows the residuals after fitting a power-law with a reflection component of $R = 1.1$. Panel (b) shows the residuals after the narrow $K\alpha$ and $K\beta$ Fe emission lines at 6.40 keV and 7.05 keV have been fitted. A broad excess is observed both red-wards and blue-wards of 6.4 keV. Panel (c) shows the residuals after the addition of a broad iron $K\alpha$ line centered at 6.4 keV. The fit in the iron K band is now good, for completeness a weak Compton shoulder to the narrow Fe $K\alpha$ line core has also been included. Note that the spectra have been re-binned by a factor of $\times 25$ for clarity.

that effects the detection of the broad iron K line.

3.4. Properties of the Reflection Component

The neutral reflection component is also very well constrained in the above model, with a best-fit value of $R = 1.1 \pm 0.2$ with a lower-limit to the cut-off energy of $E_{\text{cut}} > 170$ keV. Note that if the GSO data-point between 50–100 keV is included then $E_{\text{cut}} = 270^{+150}_{-70}$ keV (the reflection parameters are unchanged), which is consistent with the Beppo-SAX measurement (Perola et al. 2002; Balestra et al. 2004) for this source. Note the continuum photon index, cutoff energy, iron abundance, and a HXD/XIS constant normalization factor are allowed to vary independently along with the strength of the reflection hump (R). Interestingly the iron abundance of the reflector can also be constrained from the ratio of the neutral iron K edge to

the strength of the Compton hump. The iron abundance was found to be sub-Solar, with $A_{\text{Fe}} = 0.40 \pm 0.12$ relative to the Wilms et al. (2000) value. We can rule out a solar-abundance of iron with a high degree of confidence; fixing the abundance to $A_{\text{Fe}} = 1$ (but still allowing R to vary) worsened the fit statistic by $\Delta\chi^2 = 28$, as the Fe K edge in the reflection model at 7.1 keV is then too deep to model the data well. Figure 7 (top panel) shows the confidence contours of R against the iron abundance.

3.4.1. Consistency Checks

In the reflection fit, the constant cross normalization factor of the HXD over the XISFI spectrum was also allowed to vary while fitting the reflection component. Figure 7 (lower panel) shows the confidence contours between the constant and the reflection fraction (R). We find that in the best-fit described above, there is a small constant offset of 1.12 ± 0.05 between the HXD and XIS. This is consistent with calibration observations, the XIS+PIN spectrum of the Crab (Kokubun et al. 2006) also shows a factor of 1.15 ± 0.01 offset for a HXD nominal pointing and 1.13 ± 0.01 for XIS nominal (with a typical systematic uncertainty of 0.02). As one would expect, if the offset between the HXD and XIS increases, then the amount of reflection required decreases. Nonetheless the contours show that even upon allowing for some uncertainty in the constant offset between HXD and XIS, the parameters of the reflection component are well constrained. Note that the reflection parameters (and errors) quoted throughout this paper account for the uncertainty between R and the constant offset, as is shown in Figure 7.

In order to investigate the possible systematics of the HXD background on the reflection parameters, the same fits were also performed on the Suzaku data, using instead a second independent background model for the HXD/PIN, as was shown in Figure 2 (the blue data points). A reflection fraction of $R = 1.3 \pm 0.3$ was found to be consistent with the above value within the statistical errors, with the other spectral parameters unchanged. We also used the simultaneous RXTE/PCA spectrum as a mission-independent check on the strength of the reflection component. The RXTE PCU 2 data were reduced with standard extraction criteria, identical to those used in Markowitz & Edelson (2004). In fitting the RXTE spectrum, the cut-off energy was fixed at 200 keV and the iron abundance at $0.6 \times$ solar, as neither of these parameters can be constrained in the PCA data. The iron line parameters were fixed at the Suzaku XIS values, while the normalization of RXTE with respect to Suzaku is allowed to vary. With RXTE the reflection fraction was constrained to $R = 1.0^{+0.7}_{-0.4}$, while $\Gamma = 2.05 \pm 0.12$, consistent with the Suzaku observation.

Overall in the HXD band, the model extrapolated flux from 15–100 keV of MCG-5-23-16 is 1.9×10^{-10} erg cm $^{-2}$ s $^{-1}$. This is consistent with the 15–100 keV flux determined from the Swift BAT survey of 1.6×10^{-10} erg cm $^{-2}$ s $^{-1}$ (Markwardt et al. 2005) and also with a flux of 1.8×10^{-10} erg cm $^{-2}$ s $^{-1}$ obtained from Integral (Bassani et al. 2006). The consistency of the flux mea-

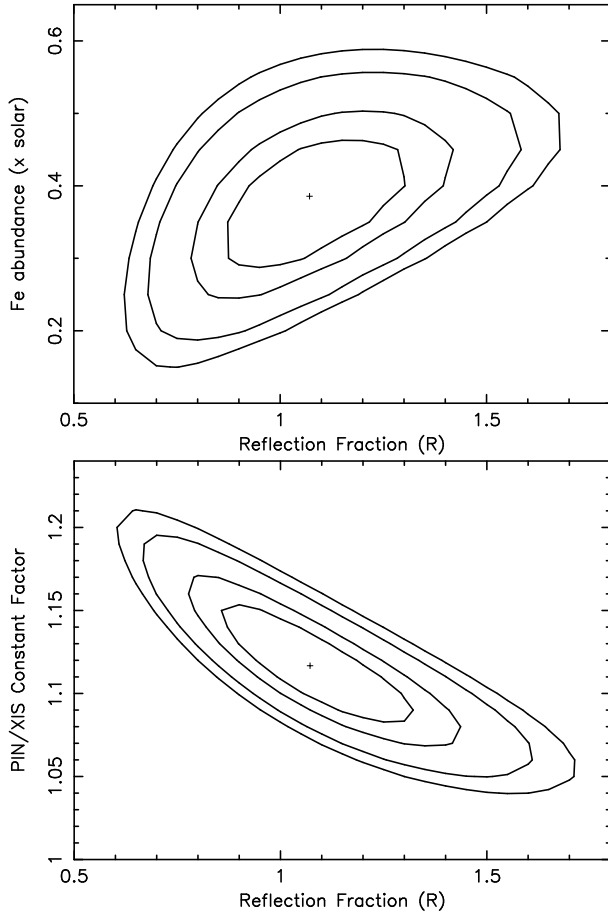


Fig. 7. Contour plots showing the 68%, 90%, 99% and 99.9% confidence levels of the reflection fraction (R). In the top panel we show R versus the iron abundance (compared to the abundances in Wilms et al. 2000), demonstrating that the iron abundance is sub-Solar. The lower panel plots R versus the constant normalization factor between the HXD/PIN and XIS FI, which shows that the constant factor is close to 1.1 and does not strongly effect the strength of the reflection component.

surements between missions is a further indication of the robustness of the Suzaku HXD data.

3.5. The Soft X-ray Spectrum

The XIS1 were added to the spectral fit to provide better constraints on the soft spectrum. The soft unabsorbed power-law component below 1 keV is found to be steep with $\Gamma = 3.1 \pm 0.3$. Furthermore the simultaneous XMM-Newton EPIC-pn and MOS data also show a soft excess, with a photon index of $\Gamma \sim 3$. In addition the XIS 1 data require an emission line at 0.92 ± 0.01 keV, with a flux of $1.5 \pm 0.2 \times 10^{-5}$ photons $\text{cm}^{-2} \text{s}^{-1}$. At this energy the line may originate from Ne IX, but could also be blended with Fe L-shell emission. There are not sufficient counts to determine if there is O K-shell emission in the XIS. However the long (100 ks) XMM-Newton RGS exposure simultaneous with the Suzaku observation shows a spectrum dominated by narrow emission lines below 1 keV, with lines from N VII Ly α , O VII (forbidden),

O VIII Ly α , O VII RRC, Ne IX (forbidden) and iron L-shell emission. The modeling of XMM-Newton RGS spectrum will be discussed in detail in a subsequent paper (Braito et al. 2006). However it seems plausible that the steep soft spectrum is the combination of a scattered power-law (with $\Gamma \sim 2$ equal to the primary continuum) superimposed on photoionized emission, similar to other Seyfert 2s (Turner et al. 1997; Sambruna et al. 2001; Kinkhabwala et al. 2002; Pounds & Page 2005; Bianchi et al. 2005). Spectral fits to the XMM-Newton EPIC and RGS data confirm that this is likely to be the case.

4. Variability of the Iron Line and Reflection Component

4.1. Short-term Variability

To test the variability of the iron line and reflection component over the timescale of the observation, the Suzaku data were split into high and low spectra for both XIS FI and HXD/PIN respectively. A threshold count rate in XIS 3 of > 3.7 counts s^{-1} and < 3.1 counts s^{-1} was used for the high and low flux spectra respectively, while spectra were then extracted with identical GTIs for XIS 0,2, HXD/PIN and the HXD/PIN background model. The XIS FI spectra were co-added as above. The resultant fluxes for the high and low spectra are then 9.9×10^{-11} erg $\text{cm}^{-2} \text{s}^{-1}$ and 7.1×10^{-11} erg $\text{cm}^{-2} \text{s}^{-1}$ respectively in the 2–10 keV band; in the 15–100 keV band the fluxes are 2.0×10^{-10} erg $\text{cm}^{-2} \text{s}^{-1}$ and 1.4×10^{-10} erg $\text{cm}^{-2} \text{s}^{-1}$. The data were fitted with the same baseline model as above.

The best fit parameters for the low and high flux spectra are shown in Table 2. In particular the input continuum normalization of the reflection component was tied at the mean value for the observation (3.2×10^{-2} photons $\text{cm}^{-2} \text{s}^{-1} \text{keV}^{-1}$ at 1 keV). Then if the reflection component varies with the continuum, an increase in the relative R value (by about 40%) with respect to the mean continuum normalization should be observed in the high flux spectrum, compared to the low spectrum. However the resulting reflection component appears to be constant for the high and low state spectra, with values of $R = 1.2 \pm 0.2$ and $R = 1.3 \pm 0.2$ respectively. Similarly the iron line fluxes of the broad and narrow components are consistent with being constant, although some variability cannot be excluded.

As a further check, the difference spectrum of the high minus low flux spectra was extracted, using both the XIS and HXD/PIN. The difference spectrum shows the variable component of the emission from MCG -5-23-16 modified by absorption, with the constant components in the spectrum being subtracted. The resulting difference spectrum was fitted extremely well with a simple absorbed power-law of photon index $\Gamma = 1.85 \pm 0.09$ and $N_{\text{H}} = 1.7 \pm 0.1 \times 10^{22} \text{cm}^{-2}$, while the fit statistic is excellent ($\chi^2/\text{dof} = 97.3/156$). Within the errors, this is consistent with the continuum parameters derived from the mean spectrum. The difference spectrum is plotted in Figure 8. There are no residuals present in the iron K band

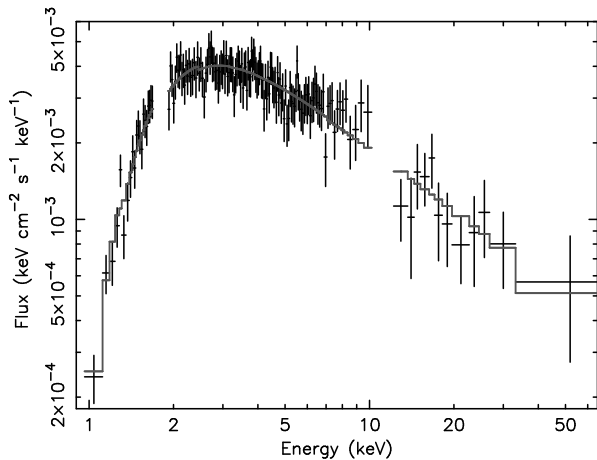


Fig. 8. The difference spectrum between high and low flux states of MCG-5-23-16 in the Suzaku observation. This can be well represented by an absorbed power-law, with no iron K emission or reflection. Thus the power-law continuum is variable, while there appears to be no variable component of the reflection spectrum.

between 6–7 keV or any excess counts in the HXD/PIN difference spectrum above 10 keV, consistent with their being no variable component to the iron line or the reflection component. From the difference spectrum, we can derive an upper-limit to any variable portion of the reflection spectrum of $R < 0.25$, or $< 20\%$ of the total reflection component. The amplitude of the reflection variability is thus smaller than the continuum variability. Note that there is no excess of counts below 1 keV in the difference spectrum, also consistent with the soft excess being constant.

4.2. Long-Term Variability of the Reflection Component

The long-term variations in the reflection component was investigated by comparing the Suzaku observation with the Beppo-SAX observation in 1998 (Perola et al. 2002; Balestra et al. 2004). The value of the reflection fraction in MCG-5-23-16 reported by Perola et al. (2002) is $R = 0.66^{+0.25}_{-0.20}$, for an inclination of $\cos\theta = 0.9$. When converted to the inclination of 45° adopted in this paper, then their reflection value is $R = 0.85^{+0.32}_{-0.25}$, which within the errors is consistent with the R value reported here from the Suzaku observation. We note that Balestra et al. (2004) find a lower R value of 0.45 (for a similar inclination of 42°) for the same Beppo-SAX observation. Note both of these papers assume solar abundances for the reflection component.

We also performed a combined fit between the 1998 Beppo-SAX observation and the 2005 Suzaku observation. The continuum parameters (e.g. photon index and cut-off energy) as well as the iron line parameters were tied between the Beppo-SAX and the Suzaku datasets, allowing only the relative continuum fluxes to vary. The input continuum normalization to the reflection component was taken as the average of the Suzaku and Beppo-SAX values. The cross normalization between SAX/PDS and SAX/MECS was fixed at 0.87. The iron abundance with

respect to Solar was fixed at 0.6, as found earlier. In this case the reflection parameters appear consistent with each other, with $R = 1.0 \pm 0.2$ and $R = 0.7 \pm 0.2$ for Suzaku and Beppo-SAX respectively. The underlying photon index is $\Gamma = 1.89 \pm 0.04$, with a high energy cut-off of 200^{+80}_{-50} keV. The flux levels of the observations are very similar, the 2–10 keV fluxes being 8.8×10^{-11} erg cm $^{-2}$ s $^{-1}$ (Suzaku) vs 9.2×10^{-11} erg cm $^{-2}$ s $^{-1}$ (Beppo-SAX). One would expect consistent reflection values, given that the object was observed at similar fluxes.

The iron line parameters measured in this paper also appear to be compatible with the values measured from previous observations; e.g. see Dewangan et al. (2003); Balestra et al. (2004) for comparison. The narrow iron K α line flux is in excellent agreement with the previous values (between $4 - 8 \times 10^{-5}$ photons cm $^{-2}$ s $^{-1}$), while the EW of the broad line measured from Suzaku (~ 60 eV) is also consistent with the previous shorter XMM-Newton observations within the errors (Dewangan et al. 2003; Balestra et al. 2004). This apparent lack of long term variability is perhaps not surprising considering this AGN has remained at a similar flux level (typically $7 - 10 \times 10^{-11}$ erg cm $^{-2}$ s $^{-1}$ in the 2–10 keV band). The source was only at a low flux level during the 1980s (see Figure 1, Mattson & Weaver 2004), as observed during the Ginga observations (Nandra & Pounds 1994) when the 2–10 keV flux reached a low of 2×10^{-11} erg cm $^{-2}$ s $^{-1}$.

5. Modeling the Reflection Component

The Suzaku spectrum clearly shows two velocity width components to the iron line profile; the narrow core being unresolved with Suzaku and even Chandra/HETG, while the broad component has a velocity width of $\sim 0.1c$. Thus it is possible that both components contribute towards the reflection spectrum, with the narrow line originating from distant matter (e.g. the putative torus) and the broad iron line from the accretion disk. Indeed one might expect an accretion disk reflector to contribute to the reflection spectrum, given the robust detection of the broad iron line.

This hypothesis was tested by modeling the 0.4–50 keV Suzaku spectrum with a dual reflection model; with an ionized disk reflector (using the REFLION model, Ross & Fabian 2005) and a neutral distant reflector (using the PEXRAV model, Magdziarz & Zdziarski 1995). The narrow iron K α , K β lines as well as the Compton shoulder were added to the model as described previously. The broad iron line is included as part of the ionized disk model. The ionized disk reflector is blurred by a Kerr metric from around a maximally rotating black hole (Laor 1991). A disk emissivity of $q = 3$ is assumed for the disk reflector, with an outer radius fixed at $400R_g$. The best fit parameters for the disk reflector are then $R = 0.95^{+0.4}_{-0.5}$ for the reflection fraction, $\theta = 42 \pm 4^\circ$ for the disk inclination angle with an inner radius truncated at $R_{\text{in}} = 20^{+45}_{-11} R_g$. The underlying continuum is $\Gamma = 1.98 \pm 0.04$, consistent with the previous fits. The ionization parameter is consistent with neutral or low ionization iron ($\xi < 60$ erg cm s $^{-1}$). Note

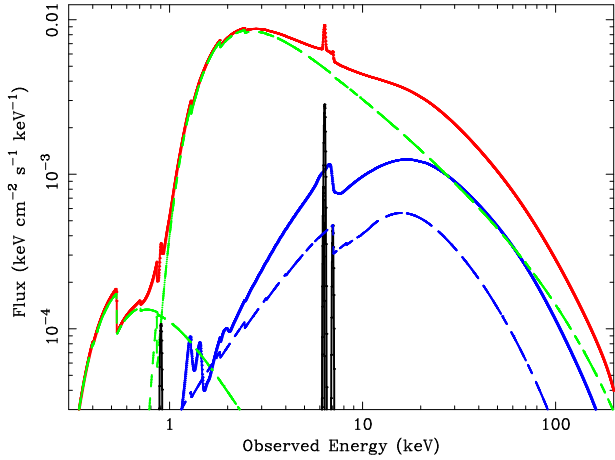


Fig. 9. Best fit dual reflection model to the Suzaku spectrum of MCG -5-23-16. The solid red line shows the total emission from the model, the dashed green line shows the primary direct cut-off power-law continuum, while at low energies, the dashed line represents the scattered power-law. The relativistically blurred ionized disk reflector is plotted with the solid blue line, while the distant reflector is shown as a dashed blue line. The narrow iron K emission lines ($K\alpha$, $K\beta$ and the Compton shoulder) are shown as solid black lines. The dual reflector model has reflection fractions of $R \sim 0.9$ and $R \sim 0.5$ for the disk and distant components respectively. The data are consistent with equal contributions from the disk and distant reflectors, within the errors.

that if we allow the disk emissivity to vary, then the best fit value is $q = 2.3^{+0.9}_{-0.5}$ and subsequently an inner disk radius extending down to $6R_g$ (the last stable orbit around a Schwarzschild black hole) or even $1.2R_g$ (for a maximal Kerr black hole) cannot be ruled out.

The iron abundance was assumed to be the same value for both the disk and distant reflection components; the best fit value found was $A_{Fe} = 0.65 \pm 0.15$. The neutral distant reflection component has a reflection fraction $R = 0.5 \pm 0.3$ (assuming a 45° inclination), while the equivalent width of the narrow iron $K\alpha$ line is 77 ± 11 eV. For a plane parallel slab, illuminated by a continuum of $\Gamma = 2$ and viewed at 45° incidence, the predicted iron line equivalent width for a neutral reflector varies between 60–70 eV (for $0.5 \times$ solar abundance), to 110 eV (for solar abundance), consistent with the measured value for the narrow iron line (Matt 2002). The overall dual reflection model is shown in Figure 9, while the fit statistic of this model fitted to the Suzaku spectrum is good ($\chi^2/\text{dof} = 1980/1878$, model 3, Table 3.). Note that a constant normalization offset factor between HXD/PIN and XIS was also included as a fit parameter, this was found to be 1.11 ± 0.04 , consistent with what was found in the previous section.

Both reflection components are required to model the Suzaku data. If the distant reflector and narrow iron line are removed and the spectrum refitted with just the ionized disk emission, then the fit statistic is much worse ($\chi^2/\text{dof} = 2261/1882$, model 4, Table 3), while the disk reflection fraction becomes rather large ($R = 1.9$). Alternatively if the disk reflector is removed (which includes the emission from the broad iron line) and the

spectrum is just fitted with the distant reflector including the narrow iron line core, then the fit statistic is also worse ($\chi^2/\text{dof} = 2027/1882$, model 2, Table 3), while the strength of the distant reflector increases to $R = 1.5 \pm 0.2$ in order to compensate for the lack of the disk reflector and broad iron line.

6. Discussion and Conclusions

The long Suzaku observation of the bright, Seyfert galaxy MCG -5-23-16 has revealed all the emission components expected in the X-ray spectrum of an obscured Seyfert galaxy in the context of AGN unified schemes (Antonucci 1993). A canonical high energy power-law ($\Gamma = 1.9 - 2.0$) continuum is observed, absorbed at low energies by Compton-thin matter and rolling over at high energies with a cut-off energy of > 170 keV. At soft X-ray energies a steep unabsorbed soft excess is observed, probably a combination of scattered power-law emission and photoionized line emission from distant gas. Such a component is common in many Seyfert 2 galaxies (Turner et al. 1997; Sambruna et al. 2001; Kinkhabwala et al. 2002; Pounds & Page 2005; Bianchi et al. 2005). Importantly, the excellent coverage of Suzaku at high energies has allowed us to obtain extremely accurate constraints on the iron K line profile and the high energy reflection component. Without a direct measurement of the reflection hump above 10 keV, the amount of reflection present in the spectrum would be uncertain, making the determination of both the underlying continuum and the iron K line parameters somewhat degenerate. Due to the broad bandpass and high signal to noise of the Suzaku data, both the broad and narrow components of the iron $K\alpha$ line as well as the reflection hump are unambiguously detected. The broad line is clearly resolved, with a velocity width of $\sigma_v = 20000$ km s $^{-1}$ (or 46000 km s $^{-1}$ FWHM), which requires emission within $\sim 100R_g$ of the putative massive black hole in MCG -5-23-16.

6.1. The Geometry and Location of the Reprocessing Matter in MCG -5-23-16

The high signal to noise of the Suzaku XIS spectrum, together with the simultaneous Chandra/HETG observation, limits the width of the narrow iron $K\alpha$ line core. The upper limit obtained with Suzaku is $\sigma_v < 2200$ km s $^{-1}$. For a black hole mass of $5 \times 10^7 M_\odot$ (Wandel & Mushotzky 1986), this corresponds to a distance of > 0.05 pc or $> 2 \times 10^4 R_g$. At this distance and given the detection of the distant reflection component observed in the HXD, a likely origin of the line is from fluorescence and scattering off material in a Compton-thick molecular torus (Ghisellini et al. 1994; Krolik et al. 1994). Alternatives to the torus could be a bi-conical outflow (Elvis 2000), or reflection off the outer radii of a warped disk (Nayakshin 2005).

Two zones of Compton thick matter may exist in MCG -5-23-16, the accretion disk being responsible for the broad iron $K\alpha$ line, while the torus is the likely candidate for the distant reprocessor. This was first suggested for this

Table 3. Comparison of iron line and reflection model fits to the mean spectrum. See text for model details.

Model	Description	χ^2/dof
1.	Neutral Reflection (pexrav) + Narrow and Broad Iron lines	1983/1879
2.	Neutral Reflection + Narrow Iron Line only	2027/1882
3.	Ionized Disk Reflection + Neutral reflection and Narrow Iron line	1980/1878
4.	Ionized Disk Reflection only	2261/1882

source by Weaver et al. (1997) on the basis of a two component model fit to the ASCA iron line profile. The dual reflection fits presented above suggest that the torus is likely Compton-thick (i.e. $N_{\text{H}} > 10^{24} \text{ cm}^{-2}$), while the iron abundance in the torus is about half the solar value. The likely geometry for MCG-5-23-16 is that we are viewing through Compton-thin material at the edge of the torus which is Compton-thick at angles along the plane of the accretion disk. This picture seems consistent with the inclination angle derived from the diskline and disk reflection fits to the broad iron line, of about 45° . Similarly Weaver & Reynolds (1998) also found inclination angles in the range $40\text{--}50^\circ$ for the iron line fits to a sample of 4 Compton-thin Seyfert 2s (including MCG-5-23-16). Indeed the fact that MCG-5-23-16 displays broad Paschen β in the infra-red (Goodrich 1994) is consistent with viewing the inner BLR through a moderate line of sight column.

An interesting question is how many of the Compton-thin Seyfert 2 galaxies show evidence for a Compton-thick reprocessor? The most detailed study to date of the high energy emission from Compton-thin Seyfert 2s was in an analysis of Beppo-SAX observations by Risaliti (2002). In the large majority of cases in this sample (17 out of 21 objects) a significant detection of Compton reflection has been found, while the authors favor a distant origin for the reflector from its apparent lack of variability. On the other hand the line of sight column densities of the Compton-thin Seyferts is too low (e.g. $N_{\text{H}} < 10^{23} \text{ cm}^{-2}$) to have sufficient efficiency for Compton down-scattering high energy photons. Thus the scenario whereby at least two zones of absorbing matter exists, with the Compton-thick zone out of the direct line of sight, would appear to be fairly commonplace in Compton-thin AGN.

In the case of MCG-5-23-16, the column density of the line of sight absorber does not appear to significantly change with time; the column density measured by Suzaku ($1.65 \pm 0.03 \times 10^{22} \text{ cm}^{-2}$) lies close to the mean value of $\sim 1.7 \times 10^{22} \text{ cm}^{-2}$ observed by ASCA, Beppo-SAX, XMM-Newton and Chandra from 1994–2001, with little scatter (Balestra et al. 2004) and it also agrees well with earlier measurements (Risaliti et al. 2002). Thus this absorber is likely to reside at large distances from the black hole (e.g. the torus or even the host galaxy) and is likely not to be clumpy. Finally we note that observations of Seyfert 2s, where the AGN appears to change from Compton-thick (i.e. reflection dominated) to Compton-thin or vice versa, also argues for the existence of at least two zones of distant absorbing matter (Matt et al. 2003). While the Compton-thick reprocessor could originate from par-

sec scale material such as the torus, it is possible that the Compton-thin X-ray absorber originates from circumnuclear gas or dust on a larger (e.g. $\sim 100 \text{ pc}$) scale within the AGN host galaxy (Maiolino et al. 1995; Malkan et al. 1998; Matt 2000; Guainazzi et al. 2005).

6.2. The Nature of the Iron K Line Emission

The lack of variability of the reflection spectrum in MCG-5-23-16 on short timescales is also consistent with part of the reflection originating in distant matter. As the high – low difference spectrum illustrates, the only variable part of the spectrum appears to be the intrinsic power-law from the disk/corona. While the distant reprocessor is not expected to vary rapidly, the lack of short-term variability of the broad line in MCG-5-23-16 is curious. The best studied example to date is MCG-6-30-15, where the relativistic iron line also appears not to vary despite strong continuum fluctuations (Vaughan & Fabian 2004), with gravitational light bending of the continuum photons near the black hole event horizon being one possible explanation (Miniutti & Fabian 2004). In MCG-5-23-16 the iron line emission is much less centrally concentrated, with the line profile characterized by an inner radius of about $\sim 20\text{--}40R_{\text{g}}$, unlike for MCG-6-30-15 where the disk emission is likely to extend into $6R_{\text{g}}$ or even $1.2R_{\text{g}}$ (Wilms et al. 2001; Fabian et al. 2002). Taking a black hole mass estimate of $5 \times 10^7 M_{\odot}$ and if the line emission originates from radii $> 20R_{\text{g}}$, then the reverberation timescale for the broad iron line will be $> 10^4 \text{ s}$, which should be observable over the Suzaku observation (of 220 ks duration). One possibility is that the continuum flux variations are not strong enough (about 40%) in this source to produce a detectable difference in the broad iron K line flux. Suzaku observations of other bright, variable Seyfert galaxies with confirmed broad iron lines will be able to address this issue. An early indication is given by the deep (350 ks) Suzaku observation of MCG-6-30-15, which despite the rapid continuum flux variability, shows no strong variations in the iron line or reflection hump with continuum flux (Miniutti et al. 2006).

Indeed the inner radius implied from the iron line profile could suggest that the inner disk may be missing or truncated in MCG-5-23-16. If the accretion rate is low enough, the innermost disk can transition to an advective dominated accretion flow or ADAF (Narayan & Yi 1995). In MCG-5-23-16 the 2–10 keV X-ray luminosity is $1.5 \times 10^{43} \text{ ergs}^{-1}$. Thus if the 2–10 keV represents $\sim 5\%$ of the bolometric output in a typical AGN (Elvis et al. 1994), then the bolometric luminosity of MCG-5-23-16 is of the order $\sim 3 \times 10^{44} \text{ ergs}^{-1}$. For a black hole mass of

$5 \times 10^7 M_{\odot}$, the accretion rate of MCG -5-23-16 is $\sim 5\%$ of the Eddington rate. Interestingly, this may be close to the transition rate between high/soft and low/hard states in Galactic black hole sources, thought to be a few percent of Eddington (Maccarone 2003). So it may be plausible that the inner disk could be truncated in MCG -5-23-16 at a few tens of gravitational radii. Conversely it is perhaps thought that most X-ray bright Seyfert galaxies are more analogous to high state black hole sources, at least based on their power density spectra (Uttley & McHardy 2005).

However an optically-thick disk may extend inwards to the last stable orbit in MCG -5-23-16. If the emissivity of the X-ray source illuminating the disk is fairly flat (e.g. varying as R^{-2}), then the disk may extend all the way to an inner radius of $6R_g$ or even $1.2R_g$. In the spectral fits, this provides an equally acceptable fit to the data. A flat emissivity profile could occur if the illuminating source is located high above the disk in the ‘‘lamp-post’’ geometry, or if the X-ray emission is dissipated from flares further out on the disk. Furthermore it is possible that matter in the innermost disk radii is close to fully ionized. The reflection spectrum of a highly ionized disk or slab can be largely featureless and resemble that of the input continuum, especially if iron becomes fully ionized down to several Thomson depths (Nayakshin et al. 2000; Ballantyne et al. 2001). In this case the inner disk radius could correspond to a characteristic radius at which the disk surface becomes fully ionized.

An alternative possibility is that the broad iron line may not even originate from the accretion disk. The emission could originate from reprocessing in either a spherical distribution of clouds (Guilbert & Rees 1988) or a bi-conical outflow (Sulentic et al. 1998; Elvis 2000). Ultra-fast outflows have been claimed in a handful of AGN, on the basis of blue-shifted high ionization iron K absorption lines or edges; e.g. PG 1211+143 (Pounds et al. 2003b), PDS 456 (Reeves et al. 2003), IC 4329a (Markowitz et al. 2006). Indeed the long December 2005 XMM-Newton observation of MCG -5-23-16 shows evidence for a variable, blue-shifted iron $K\alpha$ absorption line at 7.8 keV (Braitto et al. 2006), which could plausibly arise from such an outflow.

A broader issue is the apparent lack of broad iron lines detected in recent XMM-Newton observations of bright Seyfert galaxies. Despite the high quality of the observations, sometimes only a narrow line is present (Pounds et al. 2003a; Schurch et al. 2003; Bianchi et al. 2004). In some cases broad residuals are present in the iron K band, but the continuum curvature due to a high column warm absorber and a red-wing of a relativistic iron line are difficult to distinguish (Reeves et al. 2004; Pounds et al. 2004; Turner et al. 2005). In the example of MCG -5-23-16, with Suzaku it is clear that a broad iron line is present. However in a much shorter observation of a weaker source such a line may not be detected, or its modeling could be ambiguous where there is no bandpass above 10 keV. As discussed above, the disk lines may be weaker than expected if the inner accretion disk is close to fully ionized; this will be dependent both on the illuminating continuum and the X-ray emission geometry

(Nayakshin et al. 2000). Also if the iron abundance is less than Solar (as measured in MCG -5-23-16), the broad line will be weaker.

In AGN X-ray spectra where complex or even partial covering absorption appears to be present (e.g. NGC 3516 Turner et al. 2005, NGC 4051 Pounds et al. 2004), one of the major problems in assessing the contribution of the broad iron line is in the uncertainty in determining the underlying continuum. Suzaku presents the best capabilities of the current X-ray missions for resolving this issue, by revealing the true shape and level of the underlying continuum and reflection component through broadband observations with coverage above 10 keV, while also achieving high signal to noise (at least equal to XMM-Newton) in the iron K band. Encouragingly there appears to be a large number of hard X-ray selected AGN emerging from the Swift/BAT All Sky Survey (Markwardt et al. 2005), which could eventually number as a many as ~ 200 Type I and Type 2 AGN at a limiting flux level of $\sim 10^{-11}$ erg cm $^{-2}$ s $^{-1}$. Most of these AGN will be bright enough for detailed study both in the iron K bandpass and above 10 keV with Suzaku. These sources can form the basis of our future understanding of the iron line and Compton reflection associated with the innermost regions of AGN and for testing our understanding of Unified models and AGN evolution.

References

- Antonucci, A. 1993, ARA&A, 31, 473
 Ballantyne, D.R., Ross, R.R., & Fabian, A.C. 2001, MNRAS, 327, 10
 Balucinska-Church, M. & McCammon, D. 1992, ApJ, 400, 699
 Bassani, L. et al. 2006, ApJ, 636, L65
 Balestra, I., Bianchi, S., & Matt, G. 2004, A&A, 415, 437
 Bianchi, S., Matt, G., Balestra, I., Guainazzi, M., & Perola, G.C. 2004, A&A, 422, 65
 Bianchi, S., Miniutti, G., Fabian, A. C., & Iwasawa, K. 2005, MNRAS, 360, 380
 Boldt, E. 1987, Phys. Rep., 146, 215
 Churazov, E. et al., 2006, A&A, in press
 Dewangan, G.C., Griffiths, R.E., & Schurch, N.J. 2003, ApJ, 592, 52
 Dickey, J.M., & Lockman, F.J. 1990, ARA&A, 28, 215
 Elvis, M., et al., 1994, ApJS, 95, 1
 Elvis, M. ApJ, 2000, 545, 63
 Fabian, A.C., Rees, M.J., Stella, L., & White, N.E. 1989, MNRAS, 238, 729
 Fabian, A.C., et al., 2002, MNRAS, 335, L1
 George, I.M., & Fabian, A.C. 1991, MNRAS, 249, 352
 Ghisellini, G., Haardt, F., & Matt, G. 1994, MNRAS, 267, 743
 Goodrich, R.W., Veilleux, S., & Hill, G.J. 1994, 422, 521
 Gruber, D.E., Matteson, J.L., Peterson, L.E., & Jung, G.V. 1999, ApJ, 520, 124
 Guainazzi, M., Matt, G., Perola, G.C. 2005, A&A, 444, 119
 Guilbert, P.W. & Rees, M.J. 1988, MNRAS, 233, 475
 Kinkhabwala, A. et al., 2002, ApJ, 575, 732
 Kokubun, M. et al., 2006, PASJ, this issue
 Koyama, K. et al., 2006, PASJ, this issue
 Krolik, J.H., Madau, P., & Zycki, P.T. 1994, ApJ, 266, 653
 Kushino, A., Ishisaki, Y., Morita, U., Yamasaki, N.Y., Ishida, M., Ohashi, T., & Ueda, Y. 2002, PASJ, 54, 327

- Laor, A. 1991, *ApJ*, 376, L90
- Lightman, A.P., & White, T.R. 1988, *ApJ*, 335, L57
- Maccarone, T.J. 2003, *A&A*, 409, 697
- Magdziarz, P., & Zdziarski, A. 1995, *MNRAS*, 273, 837
- Maiolino, R., Ruiz, M., Rieke, G.H., Keller, L.D. 1995, *ApJ*, 446, 561
- Malkan, M.A., Gorjian, V., Tam, R. 1998, *ApJS*, 117,25
- Markowitz, A., & Edelson, R. 2004, *ApJ*, 617, 939
- Markowitz, A., Reeves, J.N., & Braito, V. 2006, *ApJ*, 646, 783
- Markwardt, C.B., Tueller, J., Skinner, G.K., Gehrels, N., Barthelmy, S.D., & Mushotzky, R.F. 2005, *ApJ*, 633, L77
- Matt, G. 2000, *A&A*, 355, 31L
- Matt, G. 2002, *MNRAS*, 337, 147
- Matt, G., Guainazzi, M., Maiolino, R., 2003 *MNRAS*, 342, 422
- Mattson, B.J., & Weaver, K.A. 2004, *ApJ*, 601, 771
- Miniutti, G. & Fabian, A.C. 2004, *MNRAS*, 349, 1435
- Miniutti, G. et al., 2006, *PASJ*, this issue
- Mushotzky, R. 1982, *ApJ*, 256, 92
- Mitsuda, K. et al., 2006, *PASJ*, this issue
- Nandra, K., & Pounds, K.A. 1994, *MNRAS*, 268, 405
- Nandra, K., George, I.M., Mushotzky, R.F., Turner, T.J., & Yaqoob, T. 1997, *ApJ*, 477, 602
- Narayan, R. & Yi, I. 1995, *ApJ*, 452, 710
- Nayakshin, S., Kazanas, D., & Kallman, T.R. 2000, *ApJ*, 537, 833
- Nayakshin, S. 2005, *MNRAS*, 359, 545
- Page, K.L., O'Brien, P.T., Reeves, J.N., & Turner, M.J.L. 2004, *MNRAS*, 347, 316
- Perola, G.C., Matt, G., Cappi, M., Fiore, F., Guainazzi, M., Maraschi, L., Petrucci, P.O., & Piro, L. 2002, *A&A*, 389, 802
- Pounds, K.A., Nandra, K., Stewart, G.C., George, I.M., & Fabian, A.C. 1990, *Nature*, 344, 132
- Pounds, K.A., Reeves, J.N., Page, K.L., Edelson, R., Matt, G., & Perola, G.C. 2003a, *MNRAS*, 341, 953
- Pounds, K.A., Reeves, J.N., King, A.R., Page, K.L., O'Brien, P.T., & Turner, M.J.L. 2003b, *MNRAS*, 345, 705
- Pounds, K.A., Reeves, J.N., King, A.R., & Page, K.L. 2004, *MNRAS*, 350, 10
- Pounds, K.A., & Page, K.L. 2005, *MNRAS*, 360, 1123
- Reeves, J.N., O'Brien, P.T., & Ward, M. 2003, *ApJ*, 593, L65
- Reeves, J.N., Nandra, K., George, I.M., Pounds, K.A., Turner, T.J., & Yaqoob, T. 2004, 602, 648
- Reynolds, C.S. 1997, *MNRAS*, 286, 513
- Risaliti, G. 2002, *A&A*, 386, 379
- Risaliti, G., Elvis, M., & Nicastro, F. 2002, *ApJ*, 571, 234
- Ross, R.R. & Fabian, A.C. 2005, *MNRAS*, 358, 211
- Sambruna, R.M., et al., 2001, *ApJ*, 546, L13
- Schurch, N., Warwick, R.S., Griffiths, R.S., & Sembay, S. 2003, *MNRAS*, 345, 423
- Sulentic, J.W., Marziani, P., Zwitter, T., Calvani, M., & Dultzin-Hacyan, D. 1998, *ApJ*, 501, 54
- Takahashi, T. et al., 2006, *PASJ*, this issue
- Tanaka, Y. et al. 1995, *Nature*, 375, 659
- Turner, T.J., George, I.M., Nandra, K., & Mushotzky, R.F. 1997, *ApJ*, 488, 164
- Turner, T.J., Kraemer, S.B., George, I.M., Reeves, J.N., & Bottorff, M C. 2005, 618, 155
- Uttley, P. & McHardy, I.M. 2005, *MNRAS*, 363, 586
- Vaughan, S. & Fabian, A.C. 2004, *MNRAS*, 348, 1415
- Veron, P., Lindblad, P.O., Zuiderwijk, E.J., Veron, M.P., & Adam, G. 1980, *A&A*, 87, 245
- Wandel, A., & Mushotzky, R.F. 1986, *ApJ*, 306, L61
- Weaver, K.A., & Reynolds, C.S. 1998, *ApJ*, 503, L39
- Weaver, K.A., Yaqoob, T., Mushotzky, R.F., Nousek, J., Hayashi, I., & Koyama, K. 1997, *ApJ*, 474, 675
- Wegner, G., et al., 2003, *AJ*, 126, 2268
- Wilms, J., Allen, A., McCray, R. 2000, *ApJ*, 542, 914
- Wilms, J., Reynolds, C.S., Begelman, M.C., Reeves, J., Molendi, S., Staubert, R., & Kendziorra, E. 2001, *MNRAS*, 328, L27
- Yaqoob, T., & Padmanabhan, U. 2004, *ApJ*, 604, 63